TESTING ACTIVE ROTOR CONTROL APPLICATIONS USING DLR'S MULTIPLE SWASHPLATE CONTROL SYSTEM IN THE LLF OF DNW

Rainer Bartels
rainer.bartels@dlr.de

Philip Küfmann
philip.kuefmann@dlr.de

Berend G. van der Wall
berend.vanderwall@dlr.de

Oliver Schneider
oliver.schneider@dlr.de

German Aerospace Center (DLR), Institute of Flight Systems, Braunschweig, Germany

Hermann Holthusen
hermann.holthusen@dnw.aero

Jorge Gomes
jorge.gomes@dnw.aero

Jos Postma
jos.postma@dnw.aero

German-Dutch Wind Tunnels (DNW), Marknesse, The Netherlands

Abstract

In the context of the joint research project *advanced swashplate concepts* within the nationally funded aeronautical research programm LuFo V-1, DLR's multiple swashplate control system has successfully completed its first wind tunnel tests in DNW's large low-speed facility. The main goal of the wind tunnel tests was to examine the effectiveness of several individual blade control strategies regarding noise, vibration and power reduction at different wind speeds and flight attitudes using highly instrumented Bo105-type model rotor blades as well as a newly manufactured set of model rotor blades with a more modern blade planform and profiles. The results of these tests, which for the first time included 2/rev higher harmonic control and tip path plane splitting without using actuators in the rotating frame, are a valuable addition to the data gathered from the HART- and HART II campaigns and additionally provide the opportunity to directly compare the performance of two different generations of rotor blades under otherwise identical test conditions. This paper provides an initial overview over the test setup of the rotor test rig including the multiple swashplate control system, the different measurement systems used in the wind tunnel tests, the test procedures as well as the specific blade control strategies to reach the goals. Selected first results are presented to provide an initial overview over the measurements taken and an outlook on broader, more in-depth analyses available after further data evaluation.

NOTATION

Acronyms

AHD	Airbus Helicopters Germany
AHS	American Helicopter Society
BL	baseline case (w/o active control)
BPF	blade passing frequency
BVI	blade vortex interaction
CFRP	carbon fiber-reinforced plastic
CT	computerized tomography
DLR	German Aerospace Center
DNW	German-Dutch Wind Tunnels
Dpt	data point
FRP	fiber-reinforced plastic
FTK	advanced swashplate concepts
HART	higher harmonic control aeroacoustics rotor test
HHC	higher harmonic control
IBC	individual blade control
LLF	large low-speed facility
LuFo	Luftfahrtforschungsprogramm
MBB	Messerschmitt-Bölkow-Blohm
META	multiple swashplate system
MN	minimum noise case
MV	minimum vibration case
NHC	non-harmonic control
RMS	root mean square
SKAT	scalability and risk minimization for technologies with innovative design
SPL	sound pressure level
SPL.rel	relative sound pressure level
SPR	stereo pattern recognition
TEDAS	transputer-based extendable data acquisition system
TPP	tip path plane

Symbols

a_∞	speed of sound, m/s
c;c_{eq}	(equivalent) blade chord
C_p	pressure coefficient
C_T	thrust coefficient, = $T/(\rho\pi\Omega^2R^4)$
f	frequency, Hz
FM	figure of merit
F_X	propulsive Force, fuselage drag, N
H	rotor drag, N
M_t	tip Mach number, = $\Omega R/ a_\infty$
n	n^{th} rotor harmonic
N_b	number of blades
r	radial coordinate
R	rotor radius, m
T	rotor thrust, N
V_i	induced velocity, m/s
V_∞	wind speed (tunnel), m/s
V_Z	velocity (Z-direction), m/s
W_0	virtual model weight, N
α	free-flight rotor shaft angle, deg
α_s	rotor shaft angle, deg
β	yaw angle, deg
γ	glide path angle, deg
$\Delta\alpha_{WT}$	wind tunnel correction of free-flight rotor shaft angle, deg
ϑ_n	pitch angle blade n, deg
Θ_{TW}	blade twist, deg/m
Θ_n	HHC amplitude n/rev, deg
Θ_{dip}	dip amplitude, deg
Θ_{TPP}	TPP-splitting amplitude, deg
μ	advance ratio
ρ	air density, kg/m^3
φ	roll angle, deg
Φ_n	HHC phase n/rev, deg
Φ_{dip}	dip azimuthal position, deg
Φ_{TPP}	TPP-splitting phase, deg
ω	frequency, Hz
Ω	rotor rotational frequency, Hz
Ω_{ref}	nominal rotor rotational frequency, Hz
Ψ	rotor azimuth, deg

Subscripts

nom	nominal
f	fuselage

1. INTRODUCTION

Common “conventional” active rotor control systems use actuators in the fixed frame below the swashplate for classical higher harmonic control (HHC) or have actuators within the rotor hub or on the push rods to realize individual blade control (IBC). Many of the more recent publications regarding active rotor control focus on blade-integrated actuation systems like trailing edge flaps, gurney flaps or active twist actuators for HHC and IBC [1]. Both HHC and IBC have proven to be effective regarding noise and vibration as well as power reduction in numeric simulations, wind tunnel tests and flight tests [2],[3].

In 2008 DLR introduced a novel active rotor control system: the multiple swashplate system (META). The patented META achieves IBC on rotors with more than three blades without actuators in the rotating frame [4],[5], thus combining the advantages of conventional IBC systems and the classic HHC approach [6],[7]. The META has since then been integrated into the DLR’s rotor test rig and successfully demonstrated its IBC capabilities in hover conditions [8].

In September 2015 – in the frame of the research project FTK (advanced swashplate concepts) – the META has successfully completed its first wind tunnel tests in DNW’s large low-speed facility (LLF). The main objective was to test several different IBC strategies to reduce noise emissions, power consumption and vibration levels in different simulated flight conditions (decent, cruise, high speed forward flight), which for the first time include $2/rev$ HHC and tip path plane (TPP) splitting without using actuators in the rotating frame, as well as $3-4/rev$ HHC, and non-harmonic control (NHC).

For the tests, two different sets of model rotor blades were used: first, a highly instrumented set of 40% Mach-scaled Bo105-type rotor blades, and second, a set of new model blades with a state-of-the-art planform, manufactured by DLR with support of Airbus Helicopters Germany (AHD).

The preliminary results of these tests, are a valuable addition to the data gathered from the HART [9],[10] and HART II [11],[12],[13] campaigns and additionally provide the opportunity to directly compare the performance and benefits of active rotor contol for two different generations of model rotor blades under identical test conditions.

2. TEST HARDWARE

2.1. DLR’s Rotor Test Rig

DLR’s rotor test rig (ROTEST II) consists of several assembly groups mounted on a steel frame structure. A hydraulic motor which drives the main rotor shaft via two flexible tooth belts is located in the front of the frame. The motor can deliver a maximum power of 150 kW to the rotor shaft, equaling approximately $1{,}500$ Nm of torque at a nominal rotational frequency of $\Omega_{ref} = 17.5$ Hz (110 rad/s). Hydraulic and cooling oil is delivered to the motor from an electric pump unit outside the wind tunnel via hydraulic tubing roughly 60 m in length. By this arrangement the noise produced by the pump unit does not affect the noise measurements inside the test section.

To prevent noise from the drive belts, actuators and internal components from affecting the noise measurements inside the test section, the test rig was encased in a generic, fuselage-like fairing, made of FRP and covered with sound dampening material on the inside and open cell sound absorbing foam on the outside. The fairing already been used during the HART II test, was modified prior to the tests to accommodate the META system as well as provide easy access to the rotor test rig and the META’s actuation system for check-ups and maintenance. Fig. 1 shows ROTEST II including the acoustic fairing during the preparations for the wind tunnel tests. The upper part of the fuselage encasing the META system is removed for maintenance purposes.

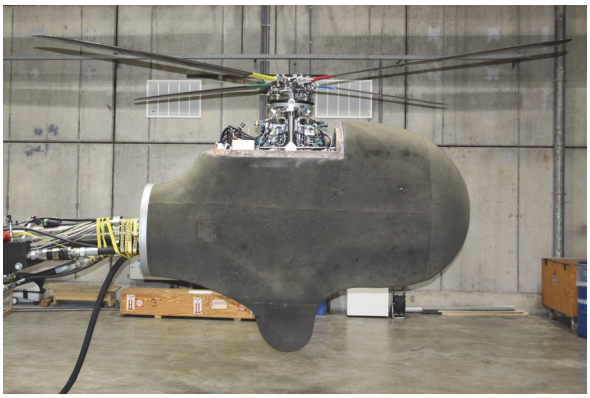

Fig. 1: ROTEST II including acoustic fairing (upper part removed for maintenance).

The DLR’s rotor test rig was mounted on an extension sting covered in acoustic dampening fabric (grey) and was positioned in the 8 m x 6 m open jet test section of the DNW’s LLF with the rotor hub at a height of approximately $dZ = +1.0$ m above the tunnel center line, see Fig. 2. The height and attidude of the model were controlled via hydraulic operation of the “torpedo” (blue) by DNW with the yaw and roll angles set to zero and a range of the rotor shaft angle α_S from $-9.6°$ to $+8.0°$. During changes of α_S, the torpedo was moved vertically to compensate for vertical shifts of the rotor hub caused by the change in attitude and to keep the rotor hub at a constant height within the test section.

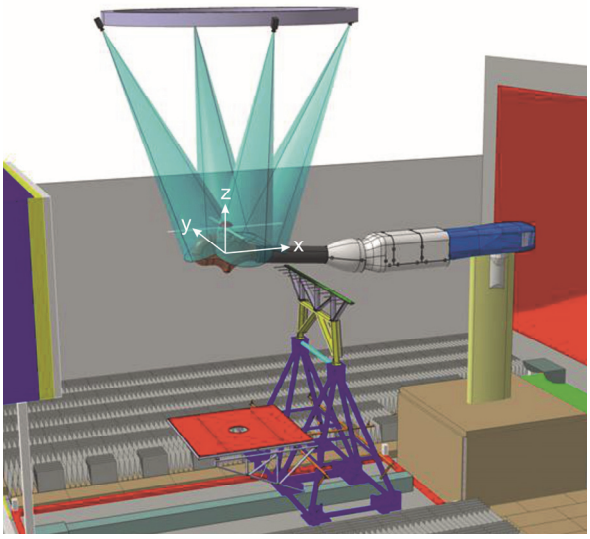

Fig. 2: CAD representation of test section including model and instrumentation.

Fig. 2 also shows the part of the instrumentation used in the tests. Above the rotor center four high-speed cameras were

mounted on a ring-shaped truss directly under the ceiling of the test section to track the movement and deformations of the individual rotor blades via stereo pattern recognition (SPR). Below the model the acoustic instrumentation, consisting of a microphone array (red) and a set of inflow microphones (green, directly below the sting) are mounted on a traversible sled which can be moved realtive to the model in flow direction.

The DLR's control container, housing the piloting rack, a dedicated META control PC interface and monitoring systems as well as additional measurement and support systems were placed outside the test section and connected to the test rig through cables run along the backside of the torpedo and inside the acoustic sting fairing. Permanent communication with the DNW's control room was maintained via short wave radio to ensure safe operations during the tests.

Details regarding the setup and operation of the measurement equipment as well as data acquisition and processing are given in section 3.

2.2. The Multiple Swashplate System (META)

The META system provides full IBC capability without the need for actuators in the rotating frame. By effectively splitting up the four-bladed model rotor in two two-bladed subrotors with their own independently controlled swashplates, it eliminates the kinematic restrictions preventing the use of arbitrary, blade invididual control signals on systems with more than three blades and a single swashplate. Fig. 3 shows a CAD representation of the META system for DLR's rotor test rig.

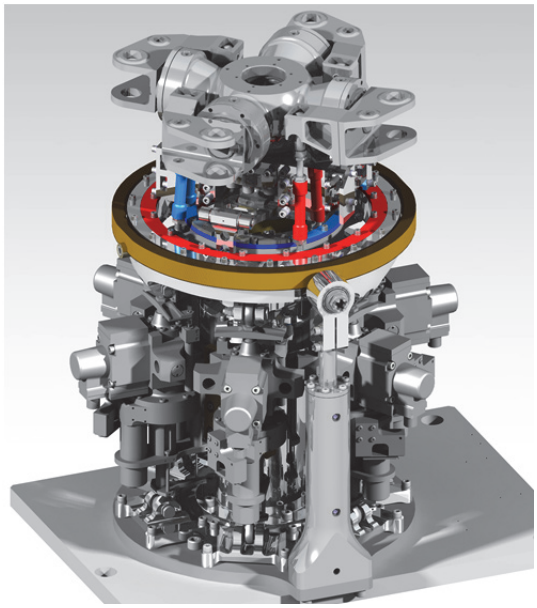

Fig. 3: CAD drawing of the META system.

The pitch links of the opposed blades 1 and 3 are connected to the outer swashplate (red) which is supported by a gimbal ring (brown) made of carbon fiber-reinforced plastic (CFRP). The other two blades (2 and 4) are controlled by the inner swashplate (blue) which is mounted on a gimbal on the rotor shaft. Each of the two swashplates is controlled by three electrohydraulic actuators mounted on the baseplate.

The electric part of the actuators has a range of motion of approximately ± 20 mm and is used for primary control of the rotor. The hydraulic piston, controlled by a servo-valve has significantly less control authority (± 4 mm) but is capable of frequencies of up to 105 Hz ($6/rev$) and is therefore used for HHC / IBC operation.

Besides higher harmonic control (HHC) with frequencies from $2-6/rev$, the META system is also capable of in-flight blade tracking as well as differential ($0/rev$) and cyclic ($1/rev$ and $2/rev$) tip-path-plane (TPP) splitting. Furthermore, even completely non-harmonic control (NHC) functions can be realized. Further details on the working principle and operation of the META can be found in [7],[8].

2.3. Model Rotor Blades

In the wind tunnel tests two different sets of model rotor blades were used. The first one is a set of 40% Mach-scaled rectangular Bo105 model rotor blades formerly used in the HART II test. It is aeroelastically scaled in a way such that the natural frequencies in terms of their non-dimensional values in n/rev are matching the full-scale blade values for the first three flapping modes, the first two lead-lag modes and the first torsion mode. Since a direct scaling cannot match the Reynolds numbers at atmospheric pressure the chord, and thus the solidity, was increased by 10%. Each blade is instrumented with strain gauges at the blade root and also at 33% radius to determine the blade load condition due to flapping, lead-lag motion and torsion. The basic data are given in Table 1.

Table 1: Basic data of Bo105 model rotor blades.

Property	Value
Rotor radius R	$2.0\ m$
Blade chord c	$0.121\ m$
Twist Θ_{TW}	$-8°/R$
Rotor system	hingeless
Rotational speed Ω_{ref}	$109\ rad/s$
1^{st} flapping frequency (F1)	$1.125/rev$
2^{nd} flapping frequency (F2)	$2.839/rev$
3^{rd} flapping frequency (F3)	$5.171/rev$
1^{st} lead-lag frequency (L1)	$0.782/rev$
2^{nd} lead-lag frequency (L2)	$4.592/rev$
1^{st} torsional frequency (T1)	$3.818/rev$

The second set, a 1:2.75 Mach-scaled version of the H145 series production blades, was designed, engineered and manufactured at DLR with support from AHD. These new model rotor blades are referred to as "FTK-blades". In order to be able to operate both sets of blades on one common rotor hub, the same hingeless blade connection as for the Bo105-blades was used. Compared to the rectangular Bo105-blades the planform of the FTK-blade features inboard tapering, a sweptback parabolic tip as well as several different airfoils (see Fig. 4).

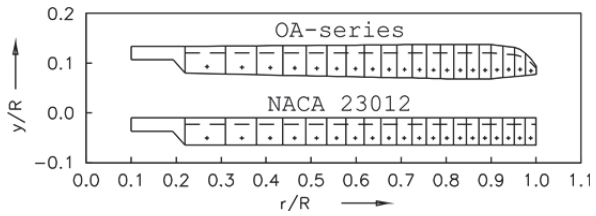

Fig. 4: Planforms of FTK-blade (top) and Bo105 model rotor blade (bottom).

Like the Bo105 model rotor blades, the FTK-blades were aeroelastically scaled to match the natural frequencies of the full-scale blades in terms of their non-dimensional values in n/rev.

This was done by building a blade equivalent beam model for the calculation by a finite element program. Starting point for the dynamic design was a rough assessment of the structural properties at a small number of 2D-sections of the blade along its radius. In an iterative process between analysis and modification of the data, a consistent refinement of the 2D-sections and improvement of the results in terms of the projected target frequencies was carried out. Table 2 shows the final result of the frequency analysis for the FTK-blades as deviations from the respective values of the original H145 blades.

Table 2: Basic data of FTK model rotor blades.

Property		Value
Rotor radius R		2.0 m
Equivalent blade chord c_{eq} (thrust-weighted)		0.124 m
Rotor system		hingeless
accuracy of 1^{st}	flapping frequency (F1)	$+2.0\%$
accuracy of 2^{nd}	flapping frequency (F2)	$+0.8\%$
accuracy of 3^{rd}	flapping frequency (F3)	-1.5%
accuracy of 4^{th}	flapping frequency (F4)	$\pm 0.0\%$
accuracy of 1^{st}	lead-lag frequency (L1)	$+16.4\%$
accuracy of 2^{nd}	lead-lag frequency (L2)	$+2.8\%$
accuracy of 1^{st}	torsional frequency (T1)	$\pm 0.0\%$

Deviations in the flapping and torsional frequencies of all modes do not exceed 2%. In contrast, the first lead-lag frequency is clearly increased, mainly as a result of the requirements for static and dynamic structural strength and the choice of materials. However, since the first lead-lag frequency has only negligible influence on $4/rev$ vibration levels and is still within the boundaries set by design guidelines for ground resonance, this value was deemed acceptable.

For the whole design process a multidisciplinary design chain was established at DLR to satisfy all boundary conditions [14]. The output of this design chain was a full 3D-model of the blade containing all information about the composite lay-up and the material properties needed. Upon manufaturing, the new FTK-blades were CT scanned at AHD to identify possible weak points in the structure. Afterwards, they were equipped with strain gauges on the blade root and then individually tested on the whirl tower at DLR. Besides measuring the blade loads, the strain gauges were also used to determine the natural frequencies in flapping, lead-lag and torsion of the FTK-blades at 0 rpm.

In Fig. 5 the frequencies of the lower eigenmodes of the FTK-blades are plotted versus the rotational speed of the rotor. The measured non-rotating frequencies of all four blades used in the wind tunnel tests are also plotted in the same figure. As can be seen, the results of these measurements are almost congruent with the target values at 0 rpm. The blade-to-blade differences of the bending modes are virtually negligible, only for torsion small variations are visible. All blades satisfy the target design and should therefore have an identical dynamic behavior compared to full-scale blades.

Even though the FTK-blade is a Mach-scaled version of the H145 rotor blade having a different blade tip speed than the full-scale Bo105-rotor, all tests were performed using the same rotational speed of $\Omega_{ref} = 110$ rad/s in order to make the results of the wind tunnel tests more comparable.

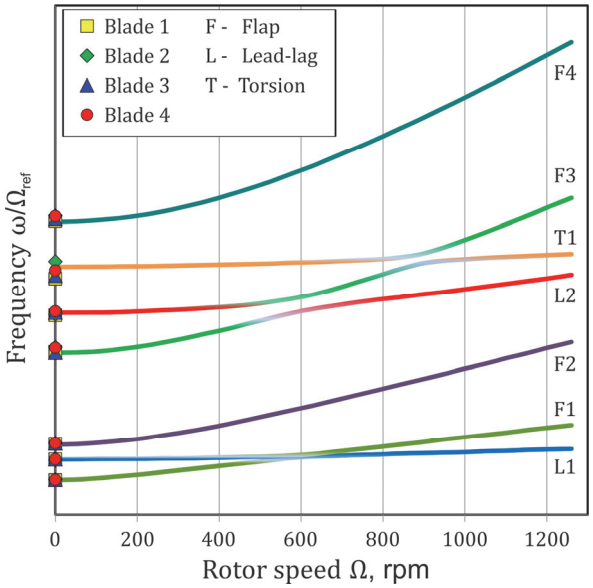

Fig. 5: Fan diagram for the FTK-blades.

3. INSTRUMENTATION AND DATA ACQUISITION

3.1. Basic Instrumentation

All forces and moments acting on the rotor were measured by DLR's six-component rotor balance located below the META system. The rotor balance features seven axial sensors, with four sensors mounted vertically, two in lateral direction and one in longitudinal direction. The sensors themselves consist of a sequence of a steady force transducer based on strain gauge measurement load cells and a dynamic force transducer consisting of a piezoresistive element. The range of the individual sensors is $\pm 10{,}000$ N both for steady and dynamic forces.

In addition to the rotor balance the rotor shaft is instrumented with two pairs of strain gauges for measurement of the moments acting on the rotor shaft as well as a torque sensor with a range of $\pm 2{,}500$ Nm.

All rotor forces and moments measured by the rotor balance as well as the signals from the blade mounted strain gauges for flapping, lead-lag and torsion were recorded by DLR's data acquisition system TEDAS I (Transputer-based extendable data acquisition system) [15] with a sampling rate of $128/rev$ and stored on hard disk. The signals were saved both as time histories and as sets of harmonic coefficients which were calculated by way of Fast Fourier Transformation (FFT) from the averaged time signals over 32 successive rotor revolutions. Additionaly, data like wind speed V_∞, main motor temperature, rotor shaft angle α_S, hydraulic pressure readings, temperatures of the bearings within the swashplates etc. were recorded for each data point.

3.2. Acoustic Measurement Equipment

The acoustic investigation performed based on two different measurement systems: a group of inflow microphones, which were installed inside of the flow of the open jet test section and a phased microphone array, which

was placed outside of the flow below the model rotor plane.

For the inflow measurements, 13 ½" condenser free-field microphones, model G.R.A.S. 40 AC, in combination with G.R.A.S. 26AF preamplifiers, were used. The microphones were equipped with ½" aerodynamic forebodies, referred as nose cones, model B&K UA 0385 [16] and mounted on a horizontal wing-shaped structure in intervals of 0.5 m. The wing itself was mounted on a traversing mechanism on the ground of the test section (see Fig. 2). By moving the traverse in streamwise direction (x-axis) and using the horizontally spaced inflow-microphones, it was possible to measure the acoustic footprint of the rotor within an area of up to 6 m upstream, 4 m downstream and ±3 m sideways of the rotor center. The spatial resolution for the streamwise movement of the traverse mechanism was set to 0.5 m to match the spacing of the microphones. For rotor shaft angles unequal to zero the resulting shift in the position of the rotor center (up to 0.3 m along the x-axis) was automatically compensated by the controls of the inflow traverse.

Special attention was given to the design of the entire structure to keep its aeroacoustic signature low and also to minimize the aerodynamic interference with the rotor. For the wind tunnel tests a smaller wing profile as mount for the microphone holders was used, to reduce possible aerodynamic interferences, when the wing is placed directly below the rotor. Moreover, no layer of acoustic foam was applied to the wing structure in order to further minimize aerodynamic interferences. Despite the missing acoustic foam, no acoustic reflections caused by the microphone wing were observed during the tests.

Further steps to reduce aerodynamic interferences included specially designed distance holders and aerodynamic fairings for mounting the microphone elements 30 cm upstream in front of the wing structure. These measures successfully eliminated the aerodynamic interference of the inflow wing onto the rotor.

The phased microphone array is equipped with 140 far-field electret microphones, model LinearX M51, which were arranged in concentric circles with a maximum diameter of 4 m. The array was mounted outside of the flow on the same traversing mechanism used for the inflow microphone wing (red square, see Fig. 2).

All acoustic data was measured with the DNW VIPER data acquisition system, which is based on 16 bit Sigma/Delta ADC technique [17]. Each VIPER frontend hosts up to 48 channels. One frontend was used for the measurement of the inflow microphones and three frontends were used for the measurement of the phased microphone array. The high accuracy synchronization between frontends was guaranteed by a hardware clock. For the investigation of the BVI noise, the output of the inflow microphones were measured in phase locked mode as well as in free run mode with a sampling frequency of 102.4 kHz. The signals of the inflow microphones were connected to the AC input of the VIPER frontend. To obtain the linear time history from the impulsive BVI noise no further high-pass filtering was applied. At the beginning of the tests, some measurements were carried out with active autorange for the gain settings to detect the absolute upper and lower level of the microphone signals. Based on the results of these preliminary measurements, the gain settings in the VIPER frontend were set to fixed values for the remainder ot the tests. This way, all measured signals had the same signal to noise ratio relative to the electrical floor level defined by the electrical noise level of the VIPER frontends and the microphone signal lines.

3.3. Stereo Pattern Recognition

The FTK-META wind tunnel test is the first campaign in which DNW deployed its upgraded Stereo Pattern Recognition (SPR) system. The sytem is designed to precisely locate and track predefined points on test objects in DNW's wind tunnels. Fluorescent markers are applied at points of interest which can subsequently be detected by a high resolution multi-camera system. The markers can either be applied using spray paint or thin stickers, such that they do not interfere with the aerodynamic behavior under investigation.

FTK- and Bo105-blades each had sixteen chord-wise pairs of fluorescent markers spray-painted onto their upper surface. Those markers, positioned along the leading and trailing edges, were used for the actual tracking, while additional supporting markers were applied to the rotor hub, the blade center line and the blade roots for global motion tracking and blade identification purposes. Fig. 6 shows an example of the marker positions on a FTK-blade.

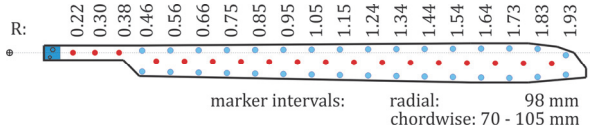

Fig. 6: Example of SPR-marker positions on FTK-blade (blue: tracking markers; red: supporting markers).

To triangulate the location of any marker the measurement volume has to be calibrated. The calibration consists of establishing the projection relations between the 3-D measurement volume to the 2-D image planes of the cameras. To determine the parameters of these relations the test section was decorated with fluorescent spheres suspended from the tunnel hall ceiling. The precise location of the spheres was subsequently determined using a theodolite. When the 3-D locations of the calibration objects are determined they can be related to their 2-D image values. This projective relation of an image and the measurement volume is not invertible, but when two or more cameras are combined triangulation becomes possible. As lenses in general tend to introduce distortions in images, lens corrections for all cameras were also determined. The most common distortions are of barrel and pincushion types. Fortunately, such lens distortions can often be corrected and therefore this was also applied for the FTK-META wind tunnel tests.

The measurement volume was covered by four *PCO-2000* cameras with a resolution of 2048 x 2048 pixels reach. These four cameras were mounted on a ring-shaped truss of approximately eight meters in diameter suspended from the ceiling, see Fig. 2. In principle a two-camera system fulfills the necessary requirements for the detection of 3-D locations from pairs of 2-D images however, a multi-camera setup allows covering a greater area or to increase triangulation accuracy.

The coordinate reconstruction is designed to be automatic and can be briefly described as follows: the four CCD camera images are searched for marker images and correspondence between the images is established using

epipolar line searches. The four cameras form a set of six stereoscopic pairs. After image correspondences have been established six point clouds are reconstructed which are appropriately averaged to form the marker coordinate results of the rotor. The marker coordinate values are returned in a more or less random order. This set of rotor marker coordinates is reordered to a predefined order using post-processing software. The reordering is performed using the local structure of the distribution of marker coordinates. The marker coordinates can then be used as a basis for geometry and deformation analysis of the rotor system.

To accurately measure the relatively fast rotating system, the whole SPR system was set up in triggered, phase-locked manner. To effectively freeze the rotor motion at the desired test conditions a Nd:YAG laser in Q-switched mode was used. The short, high intensity laser pulses with pulse widths in the order of 10 ns in duration illuminate the test section to a sufficient degree over a short time period to eliminate the high speed rotor motion, an example is shown in Fig. 7.

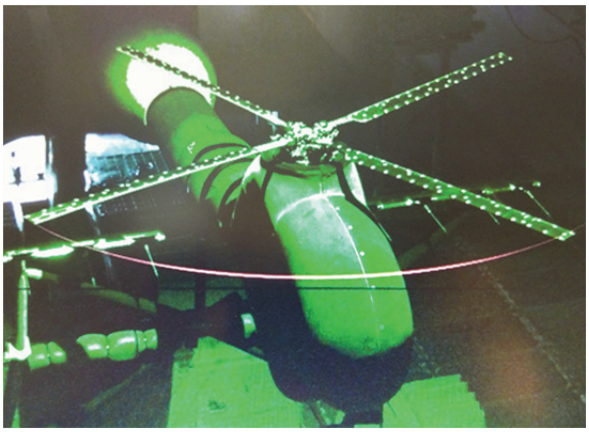

Fig. 7: Model and test section illuminated by laser pulse during SPR measurements.

A data point recording is initiated by a trigger generated by the rotor system leading to the recording of a sequence of measurements at 32 equally spaced azimuthal positions of the rotor. At each azimuthal position the four CCD camera images are acquired and subsequently processed to obtain the instantaneous 3-D coordinates of each marker on the rotor. The coordinates obtained provide a means to get quantitative information on the shape and position of individual rotor blades. The final post-processing allows the analysis of the contribution of the individual modes in flapping, lead-lag, and torsion.

3.4. Blade Pressure Measurement Equipment

Two of the Bo105-blades were instrumented with absolute pressure sensors as described in the HART II test documentation [13]. The reference blade has leading edge sensors at the 3% chord position on the upper and lower side and at radial positions of 40%, 60%, 75%, 87% and 97% radius as well as a fully instrumented section at 87% radius with 11 sensors on the upper side and six on the lower side. The blade preceding the reference blade has additional leading edge sensors at 81%, 83%, 85%, 86%, 87%, 88%, 92% and 97% radius as shown in Fig. 8.

A high-pass filtering of the leading edge sensor signals at $10/rev$ removes all fundamental steady and dynamic blade loading while keeping all the BVI fluctuations and thus is best suited to highlight the most intense interaction locations in the rotor disk. Parallel BVI, most relevant for BVI noise radiation measured by the microphones, happens on the advancing side around $50°$ azimuth and around $300°$ azimuth on the retreating side. The chordwise instrumentation allows to study the kind of pressure distribution, stall and transonic effects revealing shocks in high speed flight.

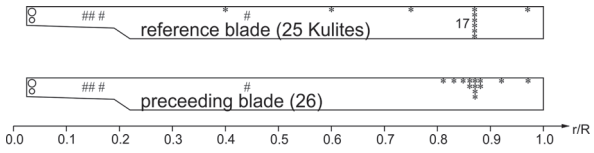

(a) Radial distribution of sensors

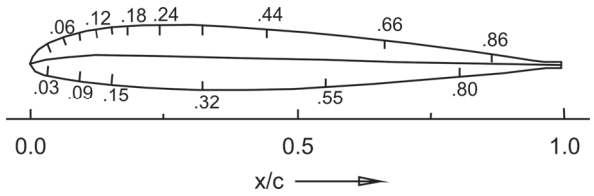

(b) Chordwise distribution of sensors at 87% radius

Fig. 8: Bo105 model rotor blade instrumentation [13].

For the recording of dynamic pressure readings, DLR's advanced TEDAS II with a sampling rate of $1024/rev$ was used in addition to the TEDAS I system. Parallel to recording the pressure readings from the Kulite sensors on the Bo105-blades, the data was displayed on a dedicated PC for online analysis during the tests.

4. TEST OVERVIEW

4.1. Test Matrix

The tests conducted at the DNW LLF included test points for three different wind speeds and flight attitudes from $7°$ descent flight at 33 m/s up to high speed level flight at 76 m/s ($\mu = 0.345$). With a few exceptions, where test points were omitted due to low priority and / or time restrictions, all test points were taken for both available model rotors. Table 3 gives an overview over the test matrix and the completed test points.

Table 3: Test matrix overview

Condition	V_∞, m/s	Bo105	FTK
Hub-drag	33-76	N/A	N/A
RPM-sweep	0	✓	✓
Hover thrust sweep	0	✓	✓
α_S-sweep for max. BVI	33	✓	✓
$2/rev$ sweeps @ 3 amps	33-76	✓	✓
$3/rev$ sweeps @ 3 amps	33-76	✓	✓
$4/rev$ sweeps @ 3 amps	33	✓	
$4/rev$ sweeps @ 3 amps	66 & 76		✓
Individual blade tracking	33	✓	✓
TPP $0/rev$ @ 7 amps	33	✓	
TPP $0/rev$ @ 5 amps	33		✓
TPP $1/rev$ @ 3 amps	33	✓	✓
Non-harmonic control	76		✓

Given the virtual model weight W_0, the virtual fuselage drag $F_{X,f}$, rotor drag H and glide angle γ of the model, the values for rotor thrust T and free-flight rotor shaft angle α can be calculated from the following equations, representing a force equilibrium in the X-Z plane:

(1)
$$\begin{aligned} F_{X,f} \cdot cos(\gamma) + H \cdot cos(\gamma - \alpha) - T \cdot sin(\gamma - \alpha) &= 0 \\ T \cdot cos(\gamma - \alpha) + F_{X,f} \cdot sin(\gamma) + H \cdot sin(\gamma - \alpha) - W_0 &= 0 \end{aligned}$$

To account for the aerodynamic differences between the open-jet test section of the wind tunnel and free flight, α_S is subsequently calculated from the free-flight shaft angle α and a correction depending on the wind speed V_∞ and thrust level of the rotor [18]:

(2)
$$\begin{aligned} \alpha_S &= \alpha + \Delta\alpha_{WT} \\ \Delta\alpha_{WT} &= 0.18 \cdot tan^{-1} \frac{C_T \cdot cos(\alpha)}{2 \cdot \left(\frac{V_\infty \cdot cos(\alpha)}{\Omega_{ref} \cdot R}\right)^2 - C_T \cdot sin(\alpha)} \end{aligned}$$

The resulting trim settings used for each flight condition are summarized in Table 4.

Table 4: Trim conditions overview

Condition	V_∞, m/s	$100 \cdot C_T$	γ	α_S
Descent flight	33	0.480	7.0°	+6.1°
Cruise flight	66	0.484	0.0°	−6.9°
High-speed flight	76	0.486	0.0°	−9.2°

The goal of the tests varied with the condition set for the respective test points. Thrust sweeps were performed in hover condition to determine the figure of merit and power required for each rotor. In the descent flight condition at 33 m/s the main focus of the tests was the reduction of BVI noise through the application of $2/rev$ and $3/rev$ IBC/HHC and TPP splitting.

Additionally, in-flight blade tracking was performed at this condition to reduce preexisting $1/rev$ imbalances on the rotor. For the two level flight conditions, cruise at 66 m/s and high-speed flight at 76 m/s the goal shifted towards vibration reduction and - to a lesser extent - the reduction of rotor power required through active rotor control, including a few test points where NHC functions were applied.

Over a course of six days in the test section with eight hours of available test time each, measurements were taken for a duration of approximately 36 hrs ("wind on" 32 hrs), resulting in a capacity utilization of nearly 75%.

4.2. General Test Procedure

At the beginning of each test sequence, the model was powered up and brought to nominal rpm ($\Omega_{ref} = 1050$ rpm) in hover condition with the META's actuators in their home position at 0 mm hydraulic stroke. After completion of startup checklists by DLR and DNW staff, the wind was turned on and V_∞ gradually increased in 5 m/s steps up to the desired wind speed. At once, DLR's main rotor operator piloted the thrust level and the rotor trim accordingly using the primary controls of the META system. At the same time, the rotor shaft pitch angle α_S was adjusted by DNW according to the desired test condition.

Depending on the wind speed V_∞ the rotor was trimmed to a zero roll- and pitch moments ($M_Y = M_X = 0$ Nm) and the precalculated values for C_T and α_S for each test condition. After the trim condition was reached, measurements were taken for the respective data point, requiring permanent communication between DLR's control container and DNW to ensure the correct sequence and completion of several measurements.

Due to time restrictions measurements with the microphone array, the inflow microphones and the SPR camera system were only taken for specific test conditions while standard data like blade loads, rotor loads and required rotor power were recorded for every data point.

4.3. Acoustic Test Procedure

The acoustic measurements were conducted in two phases. In the first, evaluation measurements with the phased microphone array were performed varying a single test parameter, like the rotor shaft angle α_S or HHC input parameters. These measurements aimed to identify the best set of parameters to achieve a reduction of BVI noise. For these evaluation measurements, the microphone array was placed at a fixed position, with the center of the array located 0.5 m upstream of the rotor center. This position proved to provide the best signal to noise ratio and the best "view" of the array towards the rotor plane. Also the interference of the airframe noise caused by the traversing mechanism was found to be minimal for this specific array location.

In the second phase, the best case selected based on online results from the array measurements was investigated more thoroughly. For the Bo105-rotor, the array results were also compared to the online results of the blade pressure measurements. For the selected case, a full microphones traverse run was performed, covering the range from 3 m upstream to 3 m downstream of the rotor center, in steps of 0.5 m. The acoustic measurements for each step took approximately 7 s and contained approximately 100 continuous rotor revolutions. For the completion of a full inflow microphone traverse run about 10 minutes were needed.

4.4. Data Analysis and Correction

Before results could be evaluated from the data acquired, almost all measurements were subject to corrections. These included corrections of rotor power required for changes of rotor and model trim during the tests as well as corrections of the vibrational loads to exclude vibrations caused by the operation of META's hydraulic actuators.

4.4.1. Correction of Measured Rotor Power

Due to the highly dynamic behavior of the model at high advance ratios in the wind tunnel, the measurements for rotor power required had to be corrected for deviations in wind speed V_∞, rotor thrust T and rotor shaft angle α_S. The correction method is based on the assumption of small perturbations, using momentum theory:

(3)
$$\begin{aligned} \Delta P &= \Delta T V_Z + T \Delta V_Z \\ &\approx \Delta T(v_i - V_\infty \alpha_S) + T(\Delta v_i - \Delta V_\infty \alpha_S - V_\infty \Delta\alpha_S) \\ \Delta T &= T_{nom} - T \\ \Delta V_\infty &= V_{\infty,nom} - V \\ \Delta\alpha_S &= \alpha_{S,nom} - \alpha_S \\ \Delta v_i &= \frac{1}{2\rho\pi R^2 V_\infty}\left(\Delta T - T\frac{\Delta V_\infty}{V_\infty}\right) \end{aligned}$$

For example, if the thrust level is less than the nominal thrust T_{nom} (and all other parameters assumed nominal),

the measured value for power required is too small, thus $\Delta P > 0$. Additionally, a correction for changes in propulsive force F_X was applied. With the power to overcome a drag force equal to F_X defined as $P_X = F_X V_\infty \cos(\alpha_S)$ the change in power due to changes in propulsive force was calculated as follows:

(4) $\Delta P_X = V_\infty \cos(\alpha_S)\Delta F_X + \Delta V_\infty F_X \cos(\alpha_S) - F_X V_\infty \sin(\alpha_S)\Delta\alpha_S$

With the assumption of small angles, this leads to:

(5) $\Delta P_X \approx V_\infty \Delta F_X + \Delta V_\infty F_X - F_X V_\infty \alpha_S \Delta\alpha_S$

Using eq. (3), (4) and (5), the corrected, effective rotor power is then calculated as $P_{eff} = P + \Delta P + \Delta P_X$. Unless noted, all data analyses and plots presented in this paper use the corrected value of P_{eff}.

4.4.2. HHC Mass Compensation

In oder to obtain the pure vibration information of the rotor system it was necessary to eliminate the influences of the two swashplates and their actuation system. When the actuators are controlled to perform dynamic pitch inputs the rotor balance also measures the loads of the accelerated masses of the swashplate structure and the actuators themselves. To compensate these loads rotational tests without blades were required. These tests were executed for each n/rev input at full rpm using three different amplitudes for each n/rev and phase sweeps in steps of $30°$. Particular focus was put on the $4/rev$ and $8/rev$ vibrations measured by the rotor balance.

The main influence was found during $4/rev$ HHC operation (see Fig. 9 and Fig. 10), since in this case all actuators perform synchronous $4/rev$ movements resulting in a collective motion of the swashplates and strong $4/rev$ as well as $8/rev$ responses in the vertical force F_Z measured by the rotor balance. The influence due to $2/rev$ and $3/rev$ harmonic inputs was found to be significantly lower, but was also compensated for during data analysis.

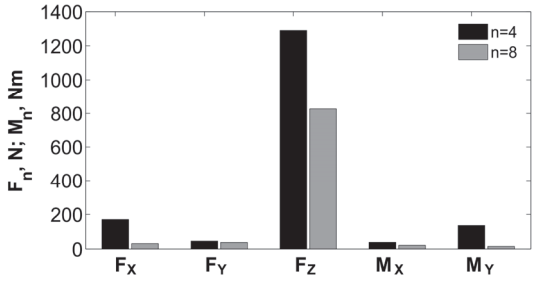

Fig. 9: Amplitudes of 4/rev and 8/rev hub loads from 4/rev HHC test w/o blades (Θ_4=0.6°).

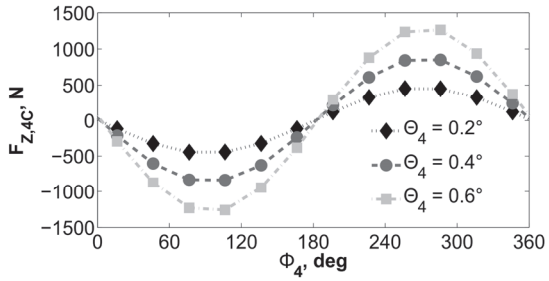

Fig. 10: Influence of 4/rev HHC inputs on cosine component of 4/rev vertical force; test w/o blades.

During data analysis, the mass compensated rotor loads were computed by subtracting the HHC mass related components from the measured loads. However, $8/rev$ loads could not be compensated since the rotor system has a resonance frequency very close to $8/rev$ and thus the corresponding loads are sometimes out of phase and sometimes in phase. For this reason $8/rev$ loads were excluded from the data analysis entirely, see section 5.3.

4.4.3. Data Processing for Inflow Microphones

First, the time data measured in the $1/rev$ acquisition mode (2048 phase locked samples per rotor revolution) are averaged over at least 100 successive rotor revolutions. From the averaged time signal containing 2048 time samples a narrow band order spectrum with 1024 lines is calculated by application of standard FFT algorithms. The 1^{st} line in this order spectrum corresponds to the rotational speed Ω_{ref} at 1050 rpm equivalent to a narrow band frequency of 17.5 Hz. For a 4-bladed rotor the 1^{st} blade passing frequency (BPF) is then equal to the 4^{th} line of the order spectrum, or a narrow band frequency of 70 Hz.

For the online assessment of the inflow microphones' signal quality the averaged time data were plotted as function of the rotor azimuth. Furthermore, the narrow band spectra were plotted showing the SPL form the 1^{st} to the 256^{th} rotor harmonic. The dominant frequency range of the Bo105 model rotor for BVI noise is located between the 24^{th} and the 160^{th} rotor harmonic (6^{th} to 40^{th} BPF harmonics). This conforms to the frequency range from 420 Hz to 2800 Hz. Due to the importance of this frequency range for the evaluation of the efficiency of noise reduction measures the narrow band RMS levels of the order spectra were integrated to an overall SPL value and plotted as function of the microphone coordinate in a color coded contour plot, the so-called carpet-plot (see section 5.4).

For comparison of individual results the level scaling for all SPL values was kept constant. The highest SPL observed during the whole test was chosen as common maximum value and applied as reference level with the value of 0dB. The dynamic range for the carpet-plots was fixed to 30dB relative to the maximum level.

The signals measured in free run acquisition mode were processed by standard FFT tools. The main advantage of this type of results was to identify noise components which were not synchronized with the rotor frequency and that otherwise would not be visible in the phase locked results based on the $1/rev$ synchronized measured data.

4.4.4. Data Processing for Out-of-Flow Phased Microphone Array

The DNW standard array processing is based on so-called "Classical Beamforming", which consists of a robust and fast processing method and therefore is especially useful for online processing [19]. The results produced by this method are normally presented in the shape of a scalar map per $1/3^{rd}$ octave frequency band (also referred to as noise-source maps). The scale of the contour plots is proportional to the SPL value within the corresponding $1/3^{rd}$ octave. These noise-source maps were used in the identification of noise source locations in the rotor plane, like the source locations of BVI noise. See for example Fig.

11, which shows the noise-source maps for the 1250 Hz $1/3^{rd}$ octave band measured during a rotor shaft angle variation of the Bo105-rotor with the locations of BVI events clearly visible in the first and fourth quadrant of the rotor disk.

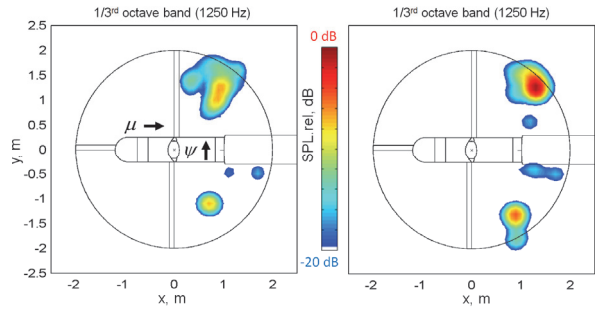

Fig. 11: Source array plots for Bo105 model rotor at α_S=3.1° (left) and α_S=6.1° (right).

Moreover, the source locations for background noise, like the model support sting or the structure of the microphone inflow traverse can be identified and the noise maps can be used for a first qualitative acoustic assessment between different test configurations. By application of a special integration technique, called power spectra integration, a narrow band spectrum was calculated, which represents the noise contribution from a single scanning area [20]. An example of the power integrated narrow band spectra is shown in Fig. 12. This plot, in which the scanning area was defined by the rotor diameter, shows a comparison between the integrated noise over the rotor area for rotor shaft angles of $3.1°$ and $6.1°$ for the Bo105-rotor.

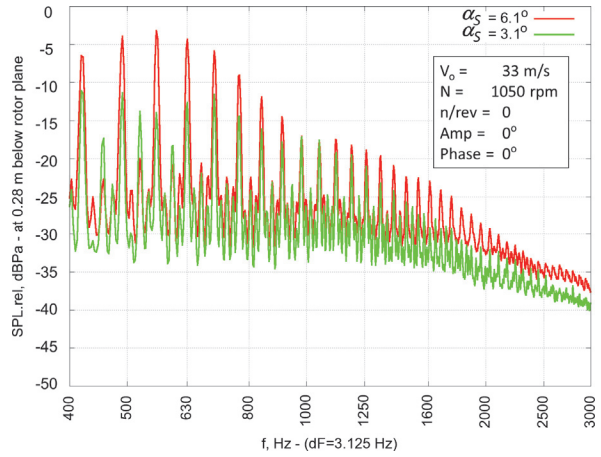

Fig. 12: Array integrated source spectra: α_S variation for maximum BVI-noise, Bo105 model rotor (baseline).

Other scanning areas of interest in the wind tunnel tests were the rotor hub, gear box, the box containing the main hydraulic valves, the support sting, and the inflow microphone wing. All these scanning areas were used to evaluate potential background noise sources.

Two major disadvantages of the classical beamforming are the dynamic range of only 12dB per frequency band and a limited capability to distinguish between background noise and side lobe noise components from neighbored scan areas. Both disadvantages can be solved using an advanced deconvolution processing technique referred to as CLEAN-SC, which has been developed for DNW by NLR [21]. For the FTK-META wind tunnel tests, the dynamic range of the results could be increased up to nearly 30dB[1]. Based on the CLEAN-SC method, the final narrow band spectra and noise-source maps provide a high signal to noise ratio, which allowed an accurate and quantitative assessment of the noise reduction measures.

5. RESULTS

5.1. Hover Performance

First, a thrust sweep was performed at hover conditions to determine the figure of merit (FM) and the power requirements for both model rotors. During these tests, the rotor thrust was gradually increased in steps of 500 N, either up to a maximum of $7{,}000$ N or until the rotor's $1/rev$ imbalance reached a level of $1{,}000$ N. For the Bo105 model rotor, the maximum allowed imbalance was reached at a thrust level of $6{,}000$ N, while the FTK-rotor could be tested up to the maximum thrust level with comparable low $1/rev$ imbalance.

As expected, the figure of merit calculated for the FTK-rotor surpassed the value for the Bo105 model rotor, especially at higher thrust levels. A qualitative comparison of the figure of merit for both rotors is shown in Fig. 13.

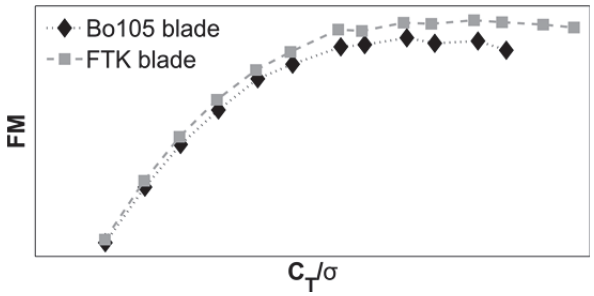

Fig. 13: Comparison of figure of merit for Bo105- and FTK-rotor.

Accordingly, the power needed to hover at a thrust of $T = 6{,}000$ N was 6.3% lower for the FTK-rotor than for the Bo105-rotor.

5.2. Rotor Power Required in Level Flight

Tests with active rotor control (HHC and IBC) for the reduction of rotor power required in forward flight were conducted for several conditions and for both rotors. In the following, the results for the high-speed level flight condition ($V_\infty = 76$ m/s, $\mu = 0.345$), where the highest power reductions were achieved, are presented.

From all HHC frequencies tested (see Table 3) the $2/rev$ input yielded the highest power savings for the Bo105- as well as for the FTK-blades. In each case, $2/rev$ amplitudes of $0.5°$, $1.0°$ and $1.5°$ were applied with phase sweeps in increments of $\Delta\Phi_2 = 30°$, while the rotor trim was maintained by adjustments of the primary controls. Fig. 14 shows the variation in P_{eff} with $2/rev$ control for the Bo105-rotor. With the exeption of a few outliers, all three curves seem to be roughly sinusoidal, with the best $2/rev$ phase settings around $230°$.

[1] The dynamic range of the presented noise-source maps was limited to 20dB for clarity.

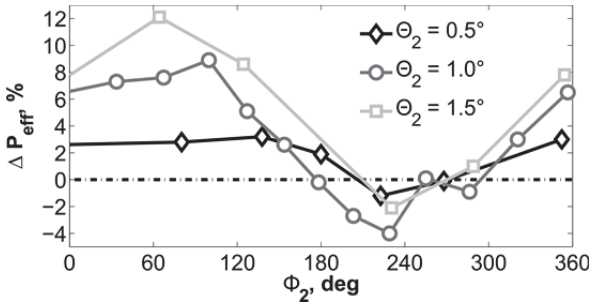

Fig. 14: Variation of effective rotor power by 2/rev HHC at 76 m/s for the Bo105 model rotor.

The highest reduction in effective rotor power (-4.0%) was measured at an amplitude of $\Theta_2 = 1.0°$ and a phase of $\Phi_2 = 229°$. Since both lower and higher $2/rev$ amplitudes ($0.5°$ and $1.5°$) did not yield higher power reductions, the optimum amplitude for power reduction in this specific case is estimated to be between those values.

For the FTK-blade, the results are depicted in Fig. 15. Here, all three amplitudes resulted in power reductions of about 2.5%, while the phase settings for the worst and best cases are roughly in agreement with the results obtained with the Bo105-rotor. The minima of all three curves lie between $\Phi_2 = 180°$ and $240°$. The highest reduction in effective rotor power (-2.7%) was measured for an amplitude of $\Theta_2 = 1.5°$, and a phase setting of $\Phi_2 = 244°$.

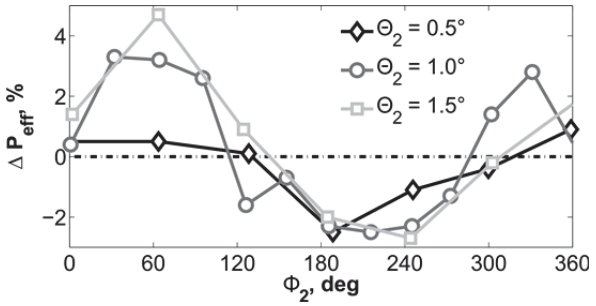

Fig. 15: Variation of effective rotor power by 2/rev HHC at 76 m/s for the FTK-rotor.

Based on the test data, the potential for rotor power reduction by means of HHC was found to be slightly lower for the modern FTK-rotor than for the Bo105-rotor. The reason for this is found in the advanced blade design of the FTK-blades (see also section 2.3). As a result the baseline level for rotor power required at $V_\infty = 76$ m/s is approximately 28% lower than for the Bo105-rotor, seemingly leaving less room for improvements in terms of power reduction.

According to simulations performed with DLR's rotor code S4, the Bo105-blades produce high levels of drag on the advancing side of the rotor disc and areas of high sectional torque contribution $C_d r M^2$ near the blade tip, resulting in high power requirements in high-speed flight. With suitable $2/rev$ HHC inputs, the blade load and thus the drag near the blade tip can be reduced in order to reduce overall power consumption. Simulations with the FTK-blades showed significantly lower drag levels near the blade tip in forward flight, mainly due to the blade's parabolic tip in combination with a high-speed airfoil on the outer section of the blade. Reductions of drag near the blade tip - and subsequently rotor power required - through application of $2/rev$ HHC were still possible, but the margins were lower than for the rectangular Bo105-blades [22].

Besides HHC, also NHC was tested for its potential to reduce rotor power required in high-speed flight. Due to limited test time, NHC [22] was tested only for the FTK-rotor at a wind speed of $V_\infty = 76$ m/s and with one amplitude setting only. The NHC-function consisted of a so-called "dip", which introduces a pitch-down movement of $\Theta_{dip} = 0.75°$ of the blade within a limited section of the rotor disc, see Fig. 16. The azimuthal location of this "dip" is determined by Φ_{dip}, which was varied in $30°$ steps during the tests.

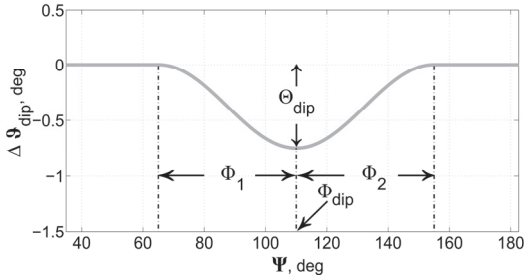

Fig. 16: Example of the NHC-function tested on the FTK-rotor.

In order to keep the frequency content of the control function and the resulting stresses on all parts of the rotor model as low as possible, half-cosine functions were used as ramps instead of discrete steps or linear functions. The width of the ramped areas is governed by the parameters Φ_1 and Φ_2, which were set to $45°$ each, resulting in an overall width of the sector affected by the NHC function of $90°$.

The results in power reduction due to the azimuth-sweeps with NHC are shown in Fig. 17. With the exception of two azimuth locations ($\Phi_{dip} = 110°$ and $\Phi_{dip} = 350°$) the influence of the NHC function on the effective rotor power is positive. The maximum reduction in effective rotor power of $\Delta P_{eff} = -3.0\%$ was measured for $\Phi_{dip} = 170°$.

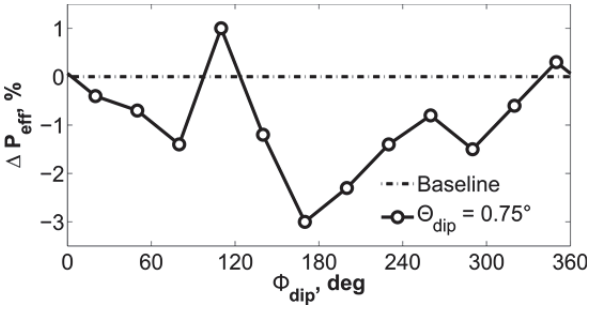

Fig. 17: Change in rotor power by NHC at 76 m/s for the FTK-rotor.

Compared to the conventional $2/rev$ HHC ($\Delta P_{eff,max} = -2.7\%$), the NHC dip yielded a slightly higher reduction of effective rotor power using less amplitude in blade pitch. The peak-to-peak value of the NHC dip was only $0.75°$, compared to $2.0°$ resulting from an amplitude of $\Theta_2 = 1.0°$ for $2/rev$ HHC. However, the vibrations introduced into the system by the rapid movements of the hydraulic actuators of the META necessary to realize the NHC dip were significantly higher than for single-frequency HHC.

5.3. Vibrations

To assess the vibration level of the model a vibration intrusion index VI_4 was defined as a weighted combination of $4/rev$ hub forces and moments according to eq. (6) using the virtual weight W_0 of the scaled model and rotor radius R to obtain non-dimensional values. $8/rev$ loads are not considered as explained in the section 4.4.2.

$$VI_4 = \frac{1}{W_0}\sqrt{\left(0.5 \cdot F_{X,4}\right)^2 + \left(0.67 \cdot F_{Y,4}\right)^2 + F_{Z,4}^2} + \frac{1}{R \cdot W_0}\sqrt{M_{X,4}^2 + M_{Y,4}^2} \quad (6)$$

Comparing the baseline case vibration index of both rotors for different flight speeds the Bo105-rotor exhibits up to 30% higher vibration levels in descent flight at 33 m/s ($\mu = 0.15$), but about 30% less at cruise condition (66 m/s, $\mu = 0.3$) than the FTK-rotor. At the high speed condition (76 m/s, $\mu = 0.345$) both rotors show similar vibration levels as shown in Fig. 18.

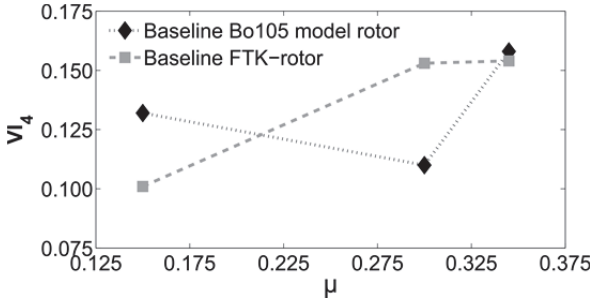

Fig. 18: Comparison of VI_4 for both model rotors at different flight conditions.

Different n/rev inputs were tested and the vibration characteristics depending on the n/rev blade pitch amplitude and phase were analyzed. For the Bo105-rotor the highest vibration reduction was found in the descent flight configuration using a $2/rev$ HHC with an amplitude of $1.5°$ at $0°$ phase. Here, the vibration index VI_4 was decreased by 77% compared to the baseline case (Fig. 19).

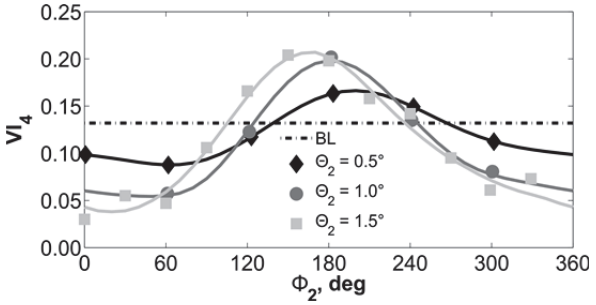

Fig. 19: Effect of 2/rev HHC on VI_4 (Bo105-rotor, μ=0.15).

A $3/rev$ control with $0.3°$ amplitude and a phase of $177°$ led to a reduction of 66% for the same flight condition (Fig. 20) - but on the other hand $3/rev$ inputs were found to produce increases of VI_4 of up to 197% ($\Theta_3 = 0.8°$, $\Phi_3 = 334°$).

Fig. 21 shows the vibration index results for the FTK-rotor for the descent flight condition and $2/rev$ HHC inputs. Compared to the baseline case, reductions of the vibration index VI_4 of up to 40% could be achieved, using an amplitude of $\Theta_2 = 1.5°$ and phase of $\Phi_2 = 359°$.

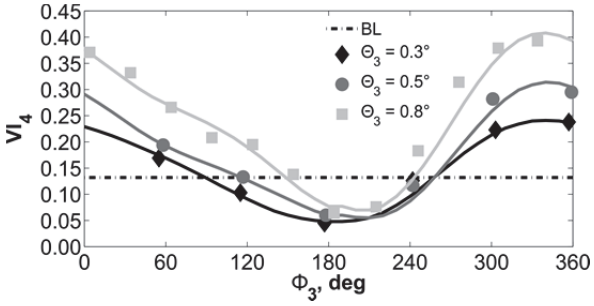

Fig. 20: Effect of 3/rev HHC on VI_4 (Bo105, μ=0.15).

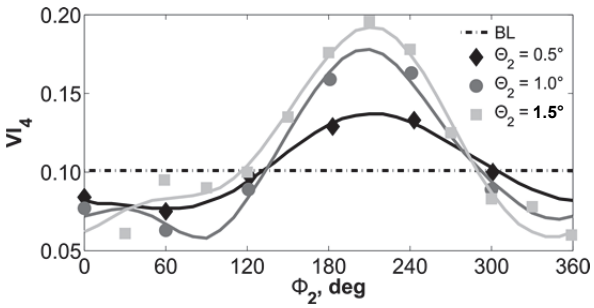

Fig. 21: Effect of 2/rev HHC on VI_4 (FTK-rotor, μ=0.15).

However, $3/rev$ HHC inputs showed significantly more influence on the vibrations of the FTK-rotor depending on amplitude and control phase, with decreases of VI_4 of up to 50% as well as maximum increases of about 284% (see Fig. 22, bottom right).

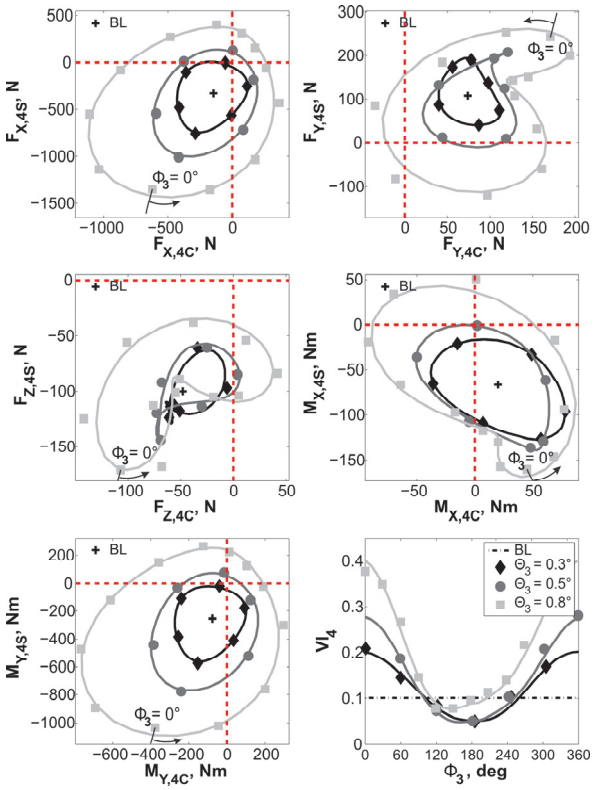

Fig. 22: Reduction of 4/rev vibration components and VI_4 for 3/rev HHC (FTK-rotor, μ=0.15).

For the FTK-rotor, it was possible to completely eliminate individual $4/rev$ load components by applying $3/rev$ inputs, see Fig. 22. By using an amplitude of $0.5°$ for example, some of the in-plane forces and moments (espedially $M_{X,4}$) could be decreased to zero, while for the same phase the vertical force $F_{Z,4}$ was reduced but still present. Higher amplitudes with a slightly different phase could further decrease $F_{Z,4}$ vibrations but in turn would increase the in-plane loads.

Fig. 23 summarizes the maximum possible vibration reductions (best case amplitudes) for all test cases and both model rotors achieved by single-frequency n/rev blade pitch inputs[2]. At some test conditions, no $4/rev$ HHC inputs were tested due to time restrictions.

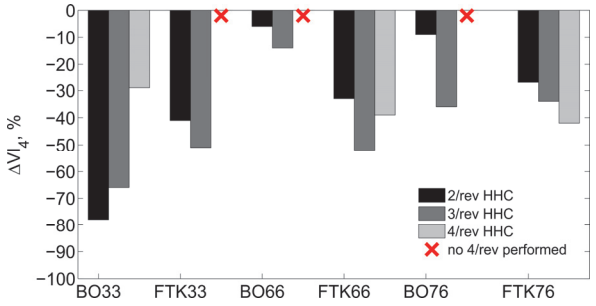

Fig. 23: Maximum vibration reductions achieved through single-frequency HHC for both model rotors.

For the Bo105-rotor, reductions of vibrational loads were possile in all test cases and the results were in agreement with the results found in [23],[24]. Since the vibration level of the Bo105-rotor is already comparatively low at $\mu = 0.30$ or 66 m/s (Fig. 18), the maximum achievable decrease in VI_4 was found to be only 10%, while for the FTK-rotor reductions of more then 50% were measured. It must be noted that in these tests only single-frequency n/rev HHC were applied using amplitude and phase sweeps. By using optimized multi-harmonic inputs improved reductions can be expected for the total vibration level VI_4.

5.4. Acoustic Results

5.4.1. Baselines and Maximum BVI Conditions

At a wind speed of $V_\infty = 33$ m/s, α_S -sweeps were performed with both rotors to find the respective maximum BVI condition and to establish the baselines for the following investigations of BVI noise reduction by means of different, single-frequency HHC inputs.

The shaft angle α_S was increased from $3.1°$ to $8.1°$ in $1°$ steps while array source maps from the out-of-flow microphone array (and in case of the Bo105-blades dynamic pressure data, see section 5.5) were analyzed regarding the locations and severity of BVI events within the rotor disk. While those array source maps were not suited for a detailed evaluation of the noise levels emitted from the rotor, they were less time consuming to produce than measuring a complete noise carpet using the inflow-traverse. This allowed for a relatively quick determination of the rotor shaft angle α_S for which the highest BVI noise was generated.

[2] The markings along the x-axis denote the combination of model rotor and V_∞ in m/s.

Comparing the two plots at $\alpha_S = 6.1°$ for the Bo105-rotor and the FTK-rotor as shown in Fig. 24, it becomes evident that the FTK-blades produce significantly less BVI-related noise than the Bo105-blades in the outer regions within the 1^{st} and 4^{th} quadrant of the rotor disk and that the locations of maximum relative sound pressure level (SPL.rel) move further inboard.

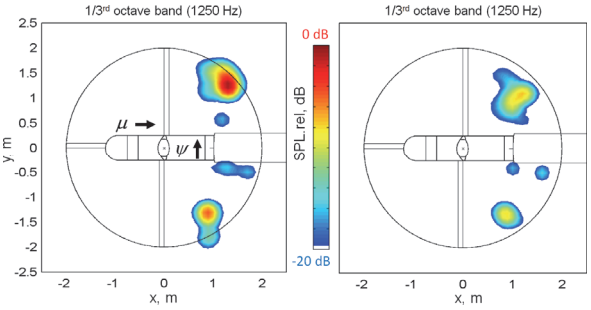

Fig. 24: Baseline array source maps for Bo105-rotor (left) and FTK-rotor (right) at max. BVI condition, α_S=6.1°.

This can be explained by the inboard tapering and the parabolic tip of the FTK-blade, both of which reduce the regions along the blade where blade-parallel BVI can occur.

After determining the maximum BVI-condition, a full traverse run with the inflow-micophones was perfomed to estabilsh a baseline noise carpet for both model rotors. Fig. 25 shows the respective noise carpets for the Bo105-rotor (left) and the FTK-rotor (right).

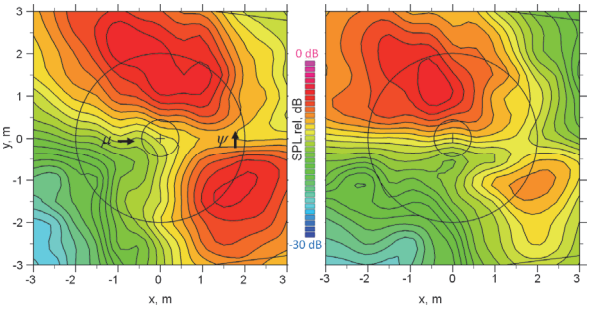

Fig. 25: Baseline noise carpets for Bo105-rotor (left) and FTK-rotor (right) at max. BVI condition, α_S=6.1°.

As expected from the array source plots, the FTK-blades show significantly lower sound pressure levels than the Bo105-blades - the region of highest relative SPL on the advancing side is considerably smaller in size and on the retreating side of the rotor the maximum value for SPL.rel is 4dB lower, than for the Bo105-blades. The difference in SPL.rel between the two rotors, averaged over all measuring points within the 6 m x 6 m plane was found to be 1.7dB in favour of the FTK-rotor.

The rotor shaft angle α_S was set to $6.1°$ for all following measurements at $V_\infty = 33$ m/s and the results presented in this section were used as baseline for all investigations regarding BVI noise reduction.

5.4.2. BVI Noise Reduction using HHC

The largest portion of the tests performed at the descent condition was concerned with the reduction of BVI-related noise emissions from the rotor by applying single-frequency

$2/rev$ and $3/rev$ HHC inputs. In order to receive results comparable to those found in the HART II test [11],[13], $3/rev$ tests were performed at amplitudes of $0.3°$, $0.5°$ and $0.8°$ while the $2/rev$ amplitudes ranged from $0.5°$ to $1.5°$ in $0.5°$ steps. For each amplitude, a phase-sweep was performed in steps of $30°$ for the highest amplitude and in steps of $60°$ for the remaining amplitudes. The array source plots were used to determine the minimum noise cases for which a full inflow microphone traverse run was performed as a follow-up.

Fig. 26 shows the resulting array source plots and noise carpets for the baseline (BL) and minimum noise (MN) cases for the Bo105-rotor. The largest reduction of BVI noise was found for a $3/rev$ amplitude of $0.8°$ and a phase setting of $\Phi_3 = 90°$. This result is consistent with results from the HART II test, where the phase settings of $\Phi_3 = 90°$ and $\Phi_3 = 300°$ yielded the best results at the same $3/rev$ amplitude.

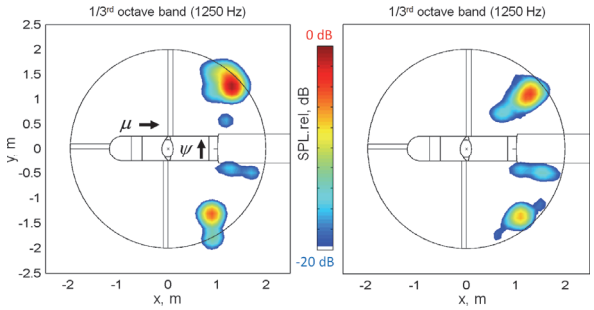

(a) [Array source plots, BL (left) and MN (right).]

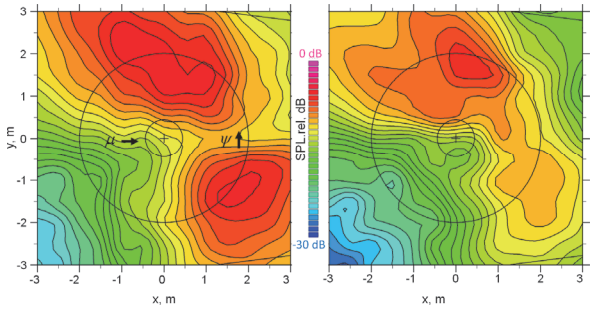

(b) [Noise carpet plots, BL (left) and MN (right).]

Fig. 26: BL (left) and BVI noise reduction through 3/rev HHC for Bo105-rotor (right) , MN: Θ_3=0.8°, Φ_3=90°.

The resulting reduction of BVI noise can be seen both in the array source plots, where the respective areas in the 1^{st} and 4^{th} quadrant have shrunk, and in the carpet plots below. Compared to the baseline case, (see Fig. 26 (b), left side), the area of high relative sound pressure level on the advancing side was considerably reduced in size and severity (-1.9dB) at MN (right), while the noisiest area on the retreating side of the rotor disk was almost completely eliminated by the HHC input (-4.5 dB), resulting in an averaged noise reduction of 2.7dB.

Measurements with the FTK-rotor showed the maximum reduction of BVI noise for a $2/rev$ HHC input with an amplitude of $\Theta_2 = 1.0°$ and a phase setting of $\Phi_2 = 0°$, see Fig. 27. Here, the resulting change in relative SPL on the retreating side is less pronounced (compared to the results of the Bo105-rotor), since the baseline noise level in that location was already relatively low. On the advancing side, however, the area of high relative SPL was reduced substantially in size and also by about 3.9dB at the location of the highest noise level, resulting in an overall reduction of BVI noise (averaged) of 2.4dB. Since the phase step for the investigations at $1°$ amplitude was $60°$ instead of $30°$, higher reductions might be found using a finer resolution.

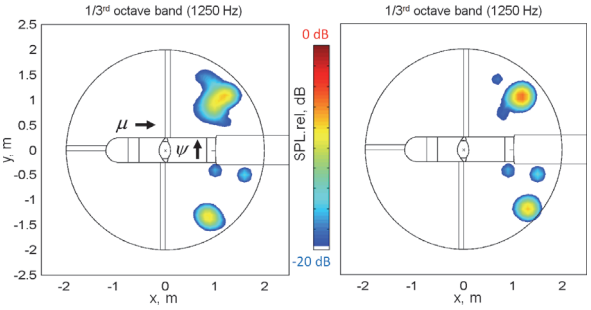

(a) [Array source plots, BL (left) and MN (right).]

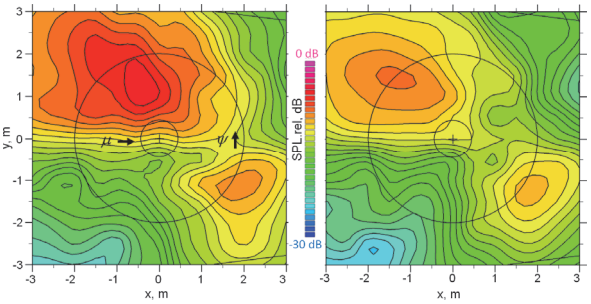

(b) [Noise carpet plots, BL (left) and MN (right).]

Fig. 27: BL (left) and BVI noise reduction through 2/rev HHC for FTK-rotor (right), MN: Θ_2=1.0°, Φ_2=0°.

As a conclusion, both model rotors exhibit significant potential for noise reduction through HHC, even though the FTK-rotor has a lower BL noise level. With the application of HHC, the average BVI noise level of the FTK-rotor could be reduced to 101.1dB, which is 2dB lower than the lowest noise level reached with the Bo105-rotor.

5.5. Blade Pressure Analysis

5.5.1. Hovering Rotor

Since only the Bo105-blades were instrumented with pressure sensors, all results presented in the following sections refer to the Bo105-rotor. During the thrust variation performed to evaluate the figure of merit FM (see section 5.1), pressure readings were recorded in parallel. Fig. 28 shows the steady part of the pressure distribution at 87% radius for this part of the tests.

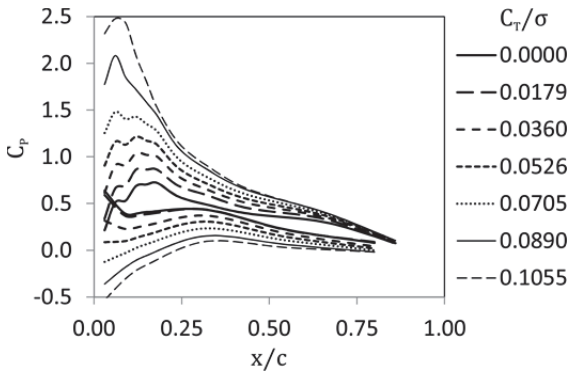

Fig. 28: Steady pressure distribution at 87% radius during hover FM evaluation (Bo105-rotor).

Even for the highest thrust level no flow separation effects can be seen, which is to be expected since the highest specific blade loading coefficient is still below $C_T/\sigma = 0.12$, a boundary usually indicating stall onset somewhere on the blade. Despite the local Mach number at this section of 0.56 even at the highest thrust no development of a local shock on the suction side can be detected, which would show up as a sharp drop of pressure within a short chordwise distance.

5.5.2. Finding the Maximum BVI Condition

At a wind speed of 33 m/s the rotor shaft angle α_S varied from $3.1°$ to $8.1°$ in $1°$ increments in order to identify the maximum BVI noise condition. Fig. 29 shows the $10/rev$ high pass filtered leading edge pressure distributions, where BVI events show up as strong fluctuations of the pressure. In Fig. 29 (a) the shaft angle setting is $3.1°$, in (b) it is $6.1°$ and in (c) it is $8.1°$.

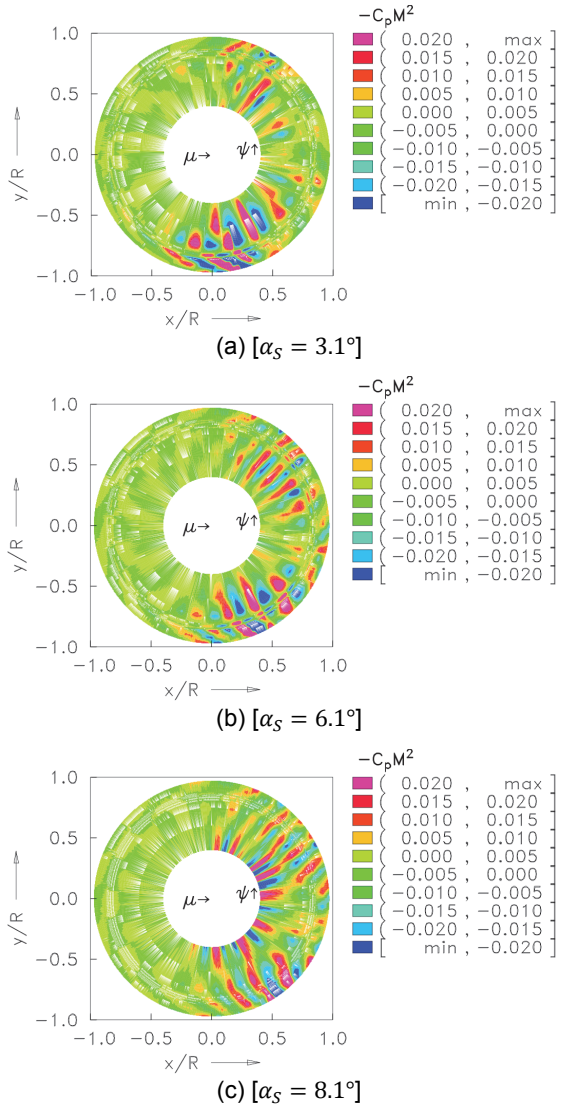

(a) [$\alpha_S = 3.1°$]

(b) [$\alpha_S = 6.1°$]

(c) [$\alpha_S = 8.1°$]

Fig. 29: Leading edge pressure fluctuations (3% chord, upper side) during variation of shaft angle. V_∞=33 m/s, C_T/σ=0.06, data 10/rev high pass filtered.

As can be seen, the BVI locations of highest intensity move continuously downstream. The most intense BVI at the parallel interaction zones around $50°$ and $300°$ azimuth are found for the case of $6.1°$ rotor shaft angle. This is in agreement with the noise data shown in Fig. 11 and Fig. 12. In the HART II test, where the same rotor was used, the maximum BVI condition was found for a rotor shaft angle of $5.4°$. However, in the FTK-META wind tunnel tests the nominal thrust was 10% higher than that used in HART II, consequently the mean induced velocities are larger, and α_S must be increased accordingly to generate the highest BVI intensity to the same locations within the rotor disk.

The BVI events around the zones of interest (parallel BVI) are compared for these three rotor shaft angle settings in Fig. 30 (a) for those on the advancing side and in (b) for those on the retreating side. The most important azimuth range zone is shaded in grey. Here, it can be seen that the $6.1°$ rotor shaft angle generates the largest BVI intensity in both of these zones and thus was identified as the maximum BVI noise generating condition.

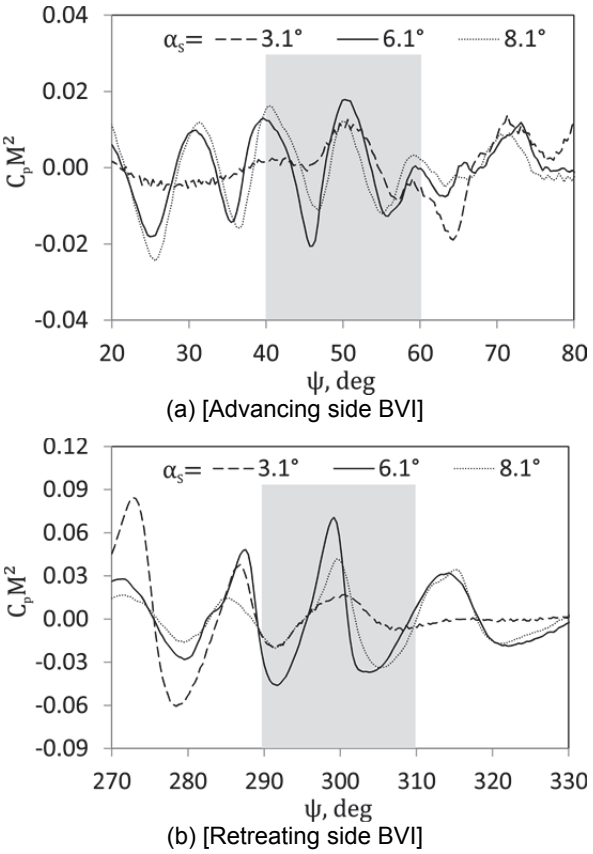

(a) [Advancing side BVI]

(b) [Retreating side BVI]

Fig. 30: Leading edge pressure fluctuations at 87% radius (3% chord, upper side) during variation of shaft angle. V_∞=33 m/s, C_T/σ=0.06, data 10/rev high pass filtered.

5.5.3. BVI Noise Reduction by 2/rev and 3/rev Control

At the operating condition of maximum BVI noise with $\alpha_S = 6.1°$ phase-sweeps were performed using $2/rev$ control with $1.5°$ amplitude and the same with $3/rev$ control with an amplitude of $0.8°$. Again, the high-frequency leading edge pressure fluctuations were used as indicator for reduced or increased BVI noise radiation and were correlated with microphone data measured in parallel, which were transformed into a power spectrum that could be directly compared with the BL reference case in the same manner as shown in Fig. 12 and Fig. 26 (a) and (b).

This comparison is first shown using the example of the leading edge pressure distributions for the minimum noise phase setting of $\Phi_2 = 90°$ for the $2/rev$ control (MN2) shown in Fig. 31 (a) and for the minimum noise phase of also $\Phi_3 = 90°$ for the $3/rev$ control shown in (b). It should be mentioned that a phase around $\psi_3 = 300°$ also reduced noise as was found during the HART II test, but here the phase of $\Phi_3 = 90°$ resulted in a larger BVI noise reduction. The comparison of the BL case in Fig. 29 (b) with MN3 in Fig. 31 (b) is in agreement with the noise measurements shown in Fig. 26.

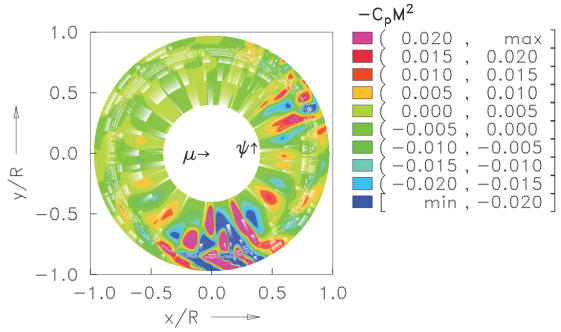

(a) [MN2: 2/rev control, $\Theta_2 = 1.5°$, $\psi_2 = 90°$]

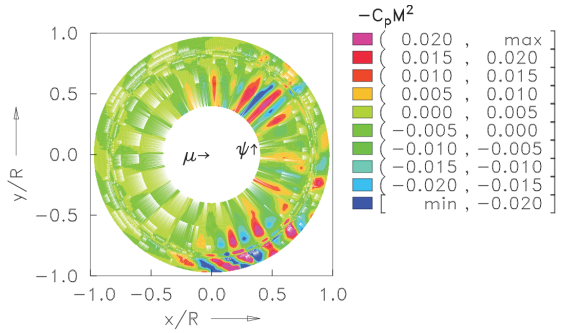

(b) [MN3: 3/rev control, $\Theta_3 = 0.8°$, $\psi_3 = 90°$]

Fig. 31: Leading edge pressure fluctuations (3% chord, upper side) at best control phase for BVI noise reduction. V_∞=33 m/s, α_S=6.1°, C_T/σ=0.06, data 10/rev high pass filtered.

More specifically, the pressure time histories at the azimuthal ranges of interest for BVI noise are given in Fig. 32 (a) for the advancing side and in (b) for the retreating side. Both active control laws significantly reduce the BVI intensity at the relevant azimuth ranges (shaded in grey), thus reducing parallel BVI intensity and consequently BVI noise radiation.

In general two principles can be used to reduce noise by means of active rotor control. The one is to increase the blade-vortex miss distance during interaction, the other is to reduce the vortex strength where it is generated. In the control laws found here to reduce noise during this test the latter principle was found to be most effective.

This can best be demonstrated by the example of the blade loading given in Fig. 33, where the $1-10/rev$ content of the blade loading at 87% radius is shown. Both the $2/rev$ and $3/rev$ minimum noise radiation conditions have a lower loading than the BL case between $\psi = 90°$ and $135°$ where the vortex is generated, thus reducing the vortex strength relative to that of the BL case.

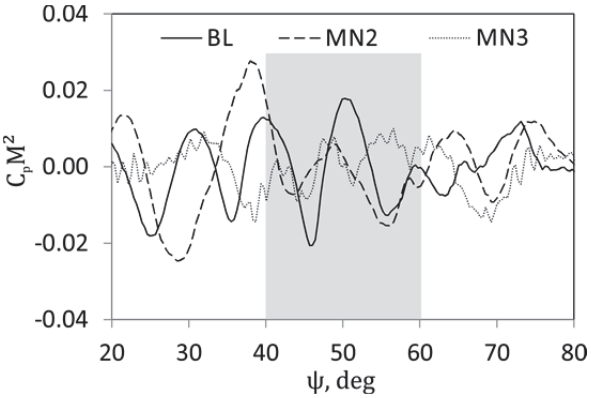

(a) [Advancing side BVI]

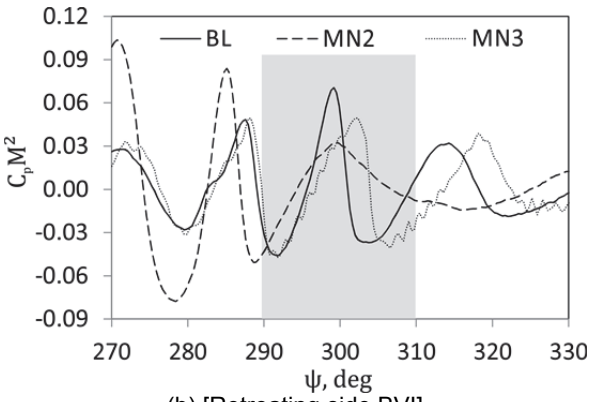

(b) [Retreating side BVI]

Fig. 32: Leading edge pressure fluctuations at 87% radius (3% chord, upper side) at best control phase for BVI noise reduction. V_∞=33 m/s, α_S=6.1°, C_T/σ=0.06, data 10/rev high pass filtered.

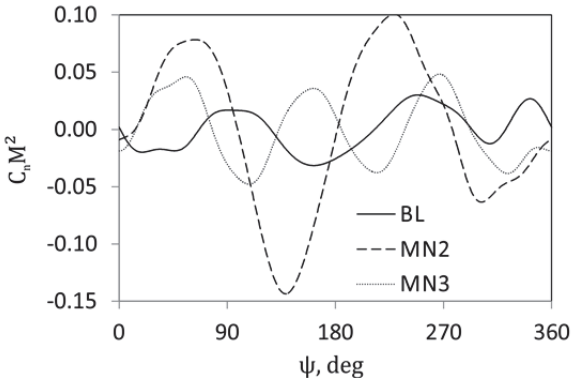

Fig. 33: Blade section loading, 1-10/rev band-pass filtered, 87% radius. V_∞=33 m/s, α_S=6.1°, C_T/σ=0.06.

5.6. SPR Results

In the following section, selected preliminary results from the SPR measurements are presented. As shown in Table 3 some of the tests conducted during the FTK-META wind tunnel tests were concerned with tip-path-plane (TPP) splitting. By splitting up the four-bladed rotor into two two-bladed “subrotors”, each controlled by one of META’s separate swashplates, differential collective or differential cyclic inputs can be used to generate two separate tip path planes.

One possible application of TPP-splitting is the reduction of BVI-generated noise by increasing the miss-distance

between blade-tip vortices moving downstream and the following blade [7],[25]. Fig. 34 shows the change in blade pitch angles relative to the baseline resulting from a cyclic ($1/rev$) TPP splitting with an amplitude of $\Theta_{TPP} = 1.0°$ and a phase of $\Phi_{TPP} = 90°$, as measured by the pitch angle sensors of the model.

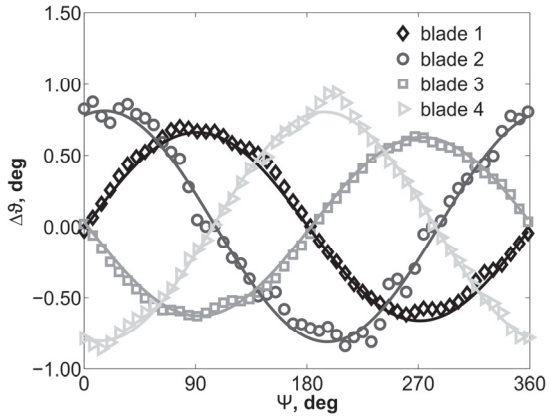

Fig. 34: Pitch angles for 1/rev TPP splitting, measurements and best-fit curves.

Compared to a regular, uniform cyclic input the pitch angles of blades 2 and 4 (controlled by the inner swashplate) are phase-shifted by $180°$. After blade 1 reaches maximum pitch at $\Psi \approx 90°$ azimuth, the next maximum pitch occurs at $\Psi \approx 180°$ for blade 4 instead of blade 2. Since the maximum $1/rev$ flap angle of a hingeless blade occurs roughly $75°$ later than the maximum blade pitch, the maximum flap angle of blades 1 and 3 should occur at an azimuth of approximately $165°$ ($345°$ for blades 2 and 4, respectively).

The deflections of the blades in z-direction, measured via SPR, are shown in Fig. 35. As expected, both "subrotors" (left and right column) develop different tip path planes due to the differential cyclic input, with maximum flap deflections at $\Psi \approx 165°$ (left) and $\Psi \approx 345°$ (right).

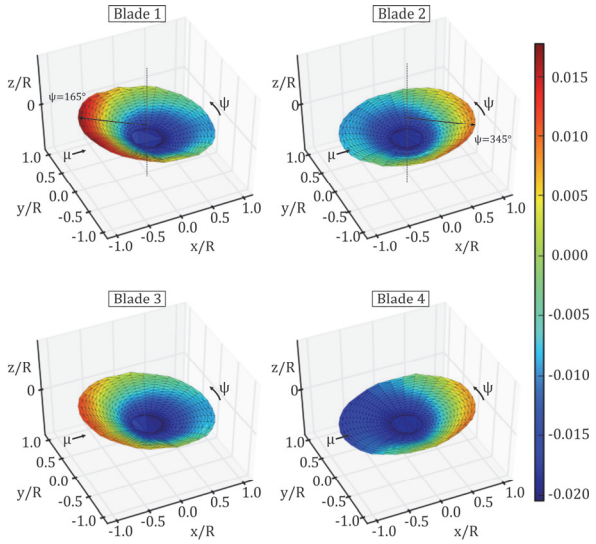

Fig. 35: SPR results for 1/rev TPP-splitting, Θ_{TPP}=1.0°, Φ_{TPP}=90°; FTK-rotor.

Another example result of DNW's new SPR system is shown in Fig. 36. Here, the plot shows the flap deviations of the blades measured during $2/rev$ HHC input with an amplitude of $1.5°$ and a phase of $180°$. Clearly visible are the minima and maxima in the blades' flapwise deflections near $\Psi \approx 0°$ and $\Psi \approx 180°$ resulting from the $2/rev$ pitch input superimposed on the primary controls.

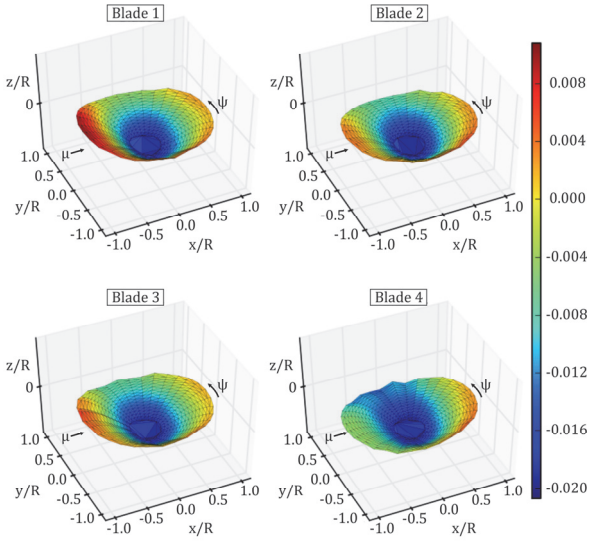

Fig. 36: SPR results for 2/rev HHC input, Θ_2=1.5°, Φ_2=180°; FTK-rotor.

The SPR results presented within this paper represent only a small portion of the possibilities for the use of the available tracking information, but already show that valuable and dependable results consistent with other measurements can be generated from the gathered raw data. As data analysis progresses, more results will become available, such as blade deformations for lead-lag or torsion eigenmodes as well as calculations of the pitch angles at different radial positions of the blade, to complement the insights gained from other measurement methods.

6. CONCLUSIONS

- In the first wind tunnel test of DLR's Multiple Swashplate System (META), the system's full-IBC capabilities were successfully applied, covering single-frequency HHC, in-flight blade tracking, collective and cyclic TPP-splitting and a form of non-harmonic blade pitch control (NHC). For the first time, $2/rev$ HHC input was realized on a rotor with four blades without actuators in the rotating frame.
- In addition to the well proven Bo105 model rotor blades, a set of new model blades (FTK-blades) was designed and manufactured at DLR with support of AHD, successfully tested in the wind tunnel and showed excellent performance.
- Reductions in effective rotor power of up to 4% through $2/rev$ HHC (Bo105-blades) and 3% through NHC (FTK-blades) were measured at a high speed flight condition. ($\mu = 0.345$).
- For both rotors, the weighted $4/rev$ vibration index VI_4 could be reduced considerably by means of single frequency HHC inputs, with maximum reductions of 77% (Bo105-rotor, $V_\infty = 33$ m/s, $2/rev$ input) and 52% (FTK-rotor, $V_\infty = 66$ m/s, $3/rev$ input). A complete elimination of single $4/rev$ in-plane vibratory loads was found to be possible using $3/rev$ control on the

FTK-rotor.

- In descent flight condition ($\mu = 0.15,\ \alpha_S = 6.1°$) BVI noise reductions for the Bo105 model rotor by up to 4.5dB were achieved by means of $3/rev$ HHC, confirming earlier findings from the HART II test both through microphone and blade pressure measurements. For the already quieter FTK-rotor, the minimum noise condition was found for a $2/rev$ HHC input, with a maximum noise reduction of 3.9dB. The averaged reduction of BVI noise measured in the 6 m x 6 m plane below the model was found to be 2.7dB (Bo105) respectively 2.4dB (FTK).
- The microphone array postprocessing proved sufficient to identify max. and min. BVI conditions, confirmed by blade pressure measurements and inflow microphone traverse runs.
- Due to their modern design, the FTK-blades showed lower potential for the reduction of rotor power required by means of IBC than the Bo105 model rotor blades. However, the results regarding vibrations and BVI noise reduction show that even with contemporary blade designs, IBC can still produce significant improvements.

Acknowledgments

The authors would like to express their gratitude towards everyone involved at DLR and DNW during the planning, preparation and execution of the FTK-META wind tunnel tests and the subsequent data analysis. Further the authors would like to thank the team at Airbus Helicopters for their support in designing the new model rotor blades used for the test and their endorsement of this publication. The tests were conducted within the framework of the national research project FTK (advanced swashplate concepts) funded by the German Federal Ministry of Economic Affairs and Energy (BMWi).

References

AC = Aeroacoustics Conference
AHS = American Helicopter Society
AST = Aerospace Science and Technology
CEAS = CEAS Aeronautical Journal
ERF = European Rotorcraft Forum
ETTC = European Telemetry and Test Conference
ICAS = International Council of the Aeronautical Sciences
JAHS = Journal of the AHS

[1] Peretz P. Friedmann. On-blade control of rotor vibration, noise, and performance: Just around the corner? *JAHS*, 4(59):1–37, 2014.

[2] Christoph Kessler. Active Rotor Control for Helicopters: Individual Blade Control and Swashplateless Rotor Designs. *CEAS*, 1(1-4):23–54, 2011.

[3] Christoph Kessler. Active Rotor Control for Helicopters: Motivation and Survey on Higher Harmonic Control. *CEAS*, 1(1-4):3–22, 2011.

[4] Berend G. van der Wall and Rainer Bartels. Helicopter rotor control device. Pat.-No.: DE-10-2006-030-089-D, Germany, 2008.

[5] Philip Küfmann. Procedure for obtaining control inputs. Pat.-No.: DE-10-2010-024-089-B4, Germany, 2013.

[6] Rainer Bartels, Philip Küfmann, and Christoph Kessler. Novel Concept for Realizing Individual Blade Control (IBC) for Helicopters. *Proceedings of the 36th ERF*, September 7-9, 2010.

[7] Philip Küfmann, Rainer Bartels, Christoph Kessler, and Berend G. van der Wall. On the Design and Development of a Multiple-Swashplate Control System for the Realization of Individual Blade Control for Helicopters. *Proceedings of the 67th Annual Forum of the AHS*, May 3-5, 2011.

[8] Philip Küfmann, Rainer Bartels, and Oliver Schneider. DLR's Multiple Swashplate Control System: Operation and Preliminary Testing. *Proceedings of the 38th ERF*, September 4-7, 2012.

[9] W. R. Splettstoesser, R. Kube, W. Wagner, U. Seelhorst, A. Boutier, F. Micheli, E. Mercker, and K. Pengel. Key Results From a Higher Harmonic Control Aeroacoustic Rotor Test (HART). *JAHS*, 42(1):58–78, 1997.

[10] R. Kube, W. R. Splettstoesser, W. Wagner, U. Seelhorst, Y. H. Yu, C. Tung, P. Beaumier, J. Prieur, G. Rahier, P. Spiegel, A. Boutier, T. F. Brooks, C. L. Burley, D. D. Boyd Jr., E. Mercker, and K. Pengel. HHC aeroacoustic rotor tests in the German-Dutch wind tunnel: Improving physical understanding and prediction codes. *AST*, 2(3):177–190, 1998.

[11] Berend G. van der Wall, B. Junker, C. L. Burley, T. F. Brooks, Y. H. Yu, C. Tung, M. Raffel, H. Richard, W. Wagner, E. Mercker, K. Pengel, H. Holthusen, P. Beaumier, and Y. Delrieux. The HART II Test in the LLF of the DNW - a major step towards rotor wake understanding. *Proceedings of the 28th ERF*, September 17-20, 2002.

[12] Marilyn J. Smith, Joon W. Lim, Berend G. van der Wall, James D. Baeder, Robert T. Biedron, Douglas D. Boyd, Buvana Jayaraman, Sung N. Jung, and Byung-Young Min. The HART II international workshop: an assessment of the state of the art in CFD/CSD prediction. *CEAS*, 4(4):345–372, 2013.

[13] Berend G. van der Wall. 2nd HHC Aeroacoustic Rotor Test (HART II) - Part I: Test Documentation. Institute Report DLR IB 111-2003/31, DLR Braunschweig, Germany, November 2003.

[14] B. van de Kamp, S. Kalow, J. Riemenschneider, H. Mainz, and R. Bartels. Multidisciplinary Design Chain for Model Rotor Blades. *To be presented at the 30th Congress of the ICAS*, September 25-30, 2016.

[15] Bernd Gelhaar, Klaus Alvermann, and F. Dzaak. A Rotor Acoustic Data Aquisition System Based On Transputers and Delta-Sigma Converters. *Proceedings of the ETTC*, June 25-27, 1991.

[16] H. Holthusen and T. Dassen. Design and testing of a low self-noise aerodynamic microphone forebody. *AIAA paper 1996-1711 (also available as NLR TP-96320L), Proceedings of the 2nd AIAA/CEAS AC*, May 6-8, 1996.

[17] H. Holthusen and H. Smit. A New Data Acquisition System for Microphone Array Measurements in Wind Tunnels. In *AIAA paper 2001-2169, Proceedings of the 7th AIAA/CEAS AC*, May 28-30, 2001.

[18] H. H. Heyson. Use of superposition in digital computers to obtain wind-tunnel interfserence factors for arbitrary configurations, with particular reference to V/STOL models. NASA Technical Report TR R-302, 1969.

[19] P. Sijtsma and S. Oerlemans. Acoustic Array Measurements of a 1:10.6 Scaled Airbus A340 Model.

AIAA paper 2004-2924, Proceedings of the 10th AIAA/CEAS AC, May 10-12, 2004.

[20] P. Sijtsma and W. R. Stoker. Determination of Absolute Contributions of Aircraft Noise Components Using Fly-over Array Measurements. *AIAA paper 2004-2958, Proceedings of the 10th AIAA/CEAS AC*, May 10-12, 2004.

[21] P. Sijtsma. CLEAN Based on Spatial Source Coherence. *AIAA paper 2007-3436, Proceedings of the 13th AIAA/CEAS AC*, May 2007.

[22] Philip Küfmann, Rainer Bartels, and Berend G. van der Wall. Localized Blade-Root IBC for Rotor-Performance Enhancement and Vibration Reduction. *Proceedings of the 40th ERF*, September 2-5, 2014.

[23] Stephen A. Jacklin, Khanh Q. Nguyen, Achim Blaas, and Peter Richter. Full-Scale Wind Tunnel Test of a Helicopter Individual Blade Control System. *Proceedings of the 50th Annual Forum of the AHS*, May 11-13, 1994.

[24] Stephen A. Jacklin, Achim Blaas, Dietrich Teves, and Roland Kube. Reduction of Helicopter BVI Noise, Vibration and Power Consumption through Individual Blade Control. *Proceedings of the 51st Annual Forum of the AHS*, pages 662–680., May 9-11, 1995.

[25] Uwe T. P. Arnold. Helicopter with Reduced Blade Vortex Interaction Noise. Pat.-No.: EP 1 428 752 B1, 2006.